

Article

Photocatalytic NO Removal by Ternary Composites $\text{Bi}_{12}\text{GeO}_{20}/\text{BiOCl}/\text{W}_{18}\text{O}_{49}$ Using a Waste Reutilization Strategy

Fei Chang ^{1,2,*} , Wenlong Bao ¹, Jiayi Li ¹, Zhongyuan Zhao ¹ and Dengguo Liu ^{3,*}

¹ School of Environment and Architecture, University of Shanghai for Science and Technology, Shanghai 200093, China; 223362030@st.usst.edu.cn (W.B.); 223362051@st.usst.edu.cn (J.L.); 213362169@st.usst.edu.cn (Z.Z.)

² School of Intelligent Emergency Management, University of Shanghai for Science and Technology, Shanghai 200093, China

³ Shanghai Environmental Monitoring Center, Shanghai 200235, China

* Correspondence: feichang@usst.edu.cn (F.C.); liudengguo@tongji.edu.cn (D.L.)

Abstract: Heterojunction creation is demonstrated as an effective strategy to enhance the transfer and separation of charge carriers, which is beneficial for subsequent photocatalytic reactions. In this study, “sea urchin-like” $\text{W}_{18}\text{O}_{49}$ was in situ-grown on the surface of $\text{Bi}_{12}\text{GeO}_{20}$ through a hydrothermal process, and the released Cl^- anions tended to produce BiOCl simultaneously. Systematical characterizations confirmed the construction of ternary composites $\text{Bi}_{12}\text{GeO}_{20}/\text{BiOCl}/\text{W}_{18}\text{O}_{49}$ (GBW), in which Type I and Z-scheme models were integrated to promote charge carrier migration and separation by combining the structural merits of both models. Under UV–visible light, the catalytic performance of the as-synthesized samples was tested in terms of NO oxidation removal. Compared to pure $\text{Bi}_{12}\text{GeO}_{20}$, the composite GBW5 showed the highest NO photocatalytic removal efficiency of 42%, which was nearly four times that of pure $\text{Bi}_{12}\text{GeO}_{20}$. These improvements were mainly due to enhanced light absorption, suitable morphological features, effective separation of charge carriers, and the boosted generation of reactive species in the GBW series. This study paves the way for the construction of $\text{Bi}_{12}\text{GeO}_{20}$ -based ternary composites using a comprehensive utilization of waste method and the employment of the composites for the photocatalytic removal of low concentrations of NO at the ppb level.

Keywords: $\text{Bi}_{12}\text{GeO}_{20}$; $\text{W}_{18}\text{O}_{49}$; BiOCl ; ternary composite; photocatalysis; NO removal



Academic Editor: Carlos Vila

Received: 10 November 2024

Revised: 23 December 2024

Accepted: 30 December 2024

Published: 14 January 2025

Citation: Chang, F.; Bao, W.; Li, J.; Zhao, Z.; Liu, D. Photocatalytic NO Removal by Ternary Composites $\text{Bi}_{12}\text{GeO}_{20}/\text{BiOCl}/\text{W}_{18}\text{O}_{49}$ Using a Waste Reutilization Strategy. *Catalysts* **2025**, *15*, 73. <https://doi.org/10.3390/catal15010073>

Copyright: © 2025 by the authors. Licensee MDPI, Basel, Switzerland. This article is an open access article distributed under the terms and conditions of the Creative Commons Attribution (CC BY) license (<https://creativecommons.org/licenses/by/4.0/>).

1. Introduction

Rapid industrialization and technological advancement are often accompanied by environmental pollution and energy consumption. After being emitted into the atmosphere, nitrogen oxides (NO_x , with NO as the major component) not only cause profound ecological damage but also pose threats to human health, leading to disasters such as acid rain and photochemical smog [1–3], as well as respiratory diseases upon inhalation [4,5]. NO at high concentrations readily oxidizes to the more toxic NO_2 in the atmosphere [1,6,7] and can be treated by conventional technologies [8–10]. However, these treatments suffer from high energy consumption, complicated equipment, and secondary pollution generation, and are, therefore, cost-ineffective for treating NO_x with low concentration and flow rate. In this context, photocatalysis emerges as a green, energy-efficient [11–13], and sustainable technology of research significance [14–16]. Under ambient conditions, it harnesses solar energy to generate reactive charge carriers and abundant radicals to eliminate toxic compounds [17]. Specifically, the oxidation of NO molecules occurs on the surface of catalysts to form NO_2^- or NO_3^- species that are converted to metabolic forms and further adsorbed by

crops, which facilitates waste utilization and circulation [18–20]. Therefore, the fabrication of an efficient photocatalytic system to remove NO is an important challenge [21,22]. In particular, the preparation of catalysts via waste reuse strategies generally provides more comprehensive support for NO_x removal research [23,24].

The semiconductor Bi₁₂GeO₂₀ exhibits unique optical and physicochemical properties, offering great potential for applications in photonic excitation, holographic imaging, optoelectronics, piezoelectrics, spatial light modulation, and photocatalysis [25–27]. However, its wide bandgap, slow charge kinetics, severe recombination of charge carriers, and poor visible light absorption greatly constrain its photocatalytic activity. Some modification strategies have been explored to enhance its photocatalytic capacity, such as morphological modulation [28], ion doping [29], carbonaceous material decoration [30], noble metal deposition [31], and heterojunction construction [32]. However, to the best of our knowledge, there are few reports on the modification of Bi₁₂GeO₂₀ for photocatalytic NO removal, suggesting considerable opportunities for further research in this area. The incorporation of another component with a narrow bandgap favors the absorption of visible light and redistribution of charge carriers in different phases, thus facilitating the enhancement of photocatalytic performance. In this context, tungsten oxide W₁₈O₄₉ is considered a fascinating candidate, possessing abundant oxygen vacancies and impressive absorption characteristics in the visible and near-infrared regions. In addition, the one-dimensional structure of W₁₈O₄₉ nanowires facilitates efficient long-distance electron transfer and sustained photocatalytic stability [33]. Moreover, W₁₈O₄₉ is able to generate high-energy hot electrons for N₂ reduction through the localized surface plasmon resonance effect [34]. Therefore, W₁₈O₄₉ with favorable physicochemical and optical merits has typically been selected to establish heterojunction composites for efficient NO removal.

During composite preparation, the dissociation of reagents provides anions and cations, which may produce different components under suitable conditions. Such processes fully utilize all species in reagents and avoid introducing external ions, thus providing an opportunity to generate heterojunction composites in a green and cost-effective manner. For this purpose, the reagent WCl₆ was adopted to produce W₁₈O₄₉, and the released Cl[−] anions react with bismuth cations in Bi₁₂GeO₂₀ lattices to generate BiOCl in situ. The obtained BiOCl, composed of {Bi₂O₂}²⁺ and Cl[−] layers arranged in a cross pattern, possesses a unique structure that expands internal space and generates an intrinsic electric field. The combined effects of internal polarization due to intrinsic magnetism and the electronegativity differences among Bi, O, and Cl facilitate the effective separation of charge carriers, thereby enhancing photocatalytic activity under ultraviolet irradiation [35,36]. As a result, these components tend to form heterojunction structures in ternary composites in situ, by which charge carriers can be further regulated and separated and photocatalytic performance may be accordingly enhanced. Moreover, the combination of Type I and Z-scheme models facilitates the migration and separation of charge carriers with relatively strong redox potentials [37–39], which may produce more active species to efficiently photocatalytically remove NO at low concentrations.

In this study, a series of ternary composites Bi₁₂GeO₂₀/BiOCl/W₁₈O₄₉ were successfully fabricated using a hydrothermal method and comprehensively characterized by using various analytical techniques. Under UV–visible light irradiation, these GBW composites were able to photocatalytically remove NO at the ppb level. The enhanced photocatalytic performance was mainly related to suitable morphologies, enhanced light absorption, strengthened separation of charge carriers, and boosted generation of reactive species. According to experimental and analytical results, the photocatalysis mechanism was proposed to be the integration of Type I and Z-scheme models in obtained composites with sufficient structural stability.

2. Results and Discussion

2.1. Microstructural and Morphological Characterization

The phase composition and crystal structures of $\text{Bi}_{12}\text{GeO}_{20}$, $\text{W}_{18}\text{O}_{49}$, BiOCl , and GBW series were analyzed by X-ray diffraction (XRD), as shown in Figure 1A. The diffraction signals at $2\theta = 21.3^\circ, 24.7^\circ, 27.7^\circ, 30.4^\circ, 32.9^\circ, 35.3^\circ, 37.5^\circ, 39.6^\circ, 41.7^\circ, 43.6^\circ, 45.5^\circ, 49.1^\circ, 52.5^\circ, 54.1^\circ, 55.7^\circ,$ and 61.9° in the XRD pattern of $\text{Bi}_{12}\text{GeO}_{20}$ correspond well to the (211), (220), (310), (222), (321), (400), (411), (024), (332), (422), (134), (125), (035), (600), (532), and (631) crystal planes of tetragonal $\text{Bi}_{12}\text{GeO}_{20}$ (Joint Committee on Powder Diffraction Standards, JCPDS File NO. 77-0861) [27], respectively. The XRD pattern of $\text{W}_{18}\text{O}_{49}$ is in good accordance with the monoclinic phase (JCPDS File NO. 05-0392) [33]. However, diffraction peaks of $\text{W}_{18}\text{O}_{49}$ are unobservable in GBW composites, mainly due to their trace amount and uniform distribution. However, some extra peaks emerged in the composite GBW3 and became enhanced with an increase in WCl_6 addition. By comparison, these extra peaks are derived from the tetragonal matlockite BiOCl phase (JCPDS File NO. 06-0249) [35]. For further identification, NaCl was adopted as the Cl source to replace WCl_6 to produce a series of binary composites GB that clearly includes diffraction peaks from both components $\text{Bi}_{12}\text{GeO}_{20}$ and BiOCl , as shown in Figure S2. Therefore, during the synthesis of $\text{W}_{18}\text{O}_{49}$, the component BiOCl was simultaneously produced by combining Bi^{3+} cations on the surface of $\text{Bi}_{12}\text{GeO}_{20}$ and Cl^- anions from WCl_6 , fully utilizing the different species contained. The other different structural parameters were investigated by using XRD patterns, which included lattice parameters, c/a ratio, density ρ (g/cm^3), and unit cell volume v (\AA^3) [40,41]. For $\text{Bi}_{12}\text{GeO}_{20}$: $a = 10.153$, $b = 10.153$, $c = 10.153$, $\alpha = 90.00$, $\beta = 90.00$, $c/a = 1.000$, volume $v = 1046.6$, density $\rho = 9.201$. For $\text{W}_{18}\text{O}_{49}$: $a = 18.318$, $b = 3.783$, $c = 14.028$, $\alpha = 90.00$, $\beta = 115.21$, $c/a = 0.766$, volume $v = 879.5$, and density $\rho = 7.727$.

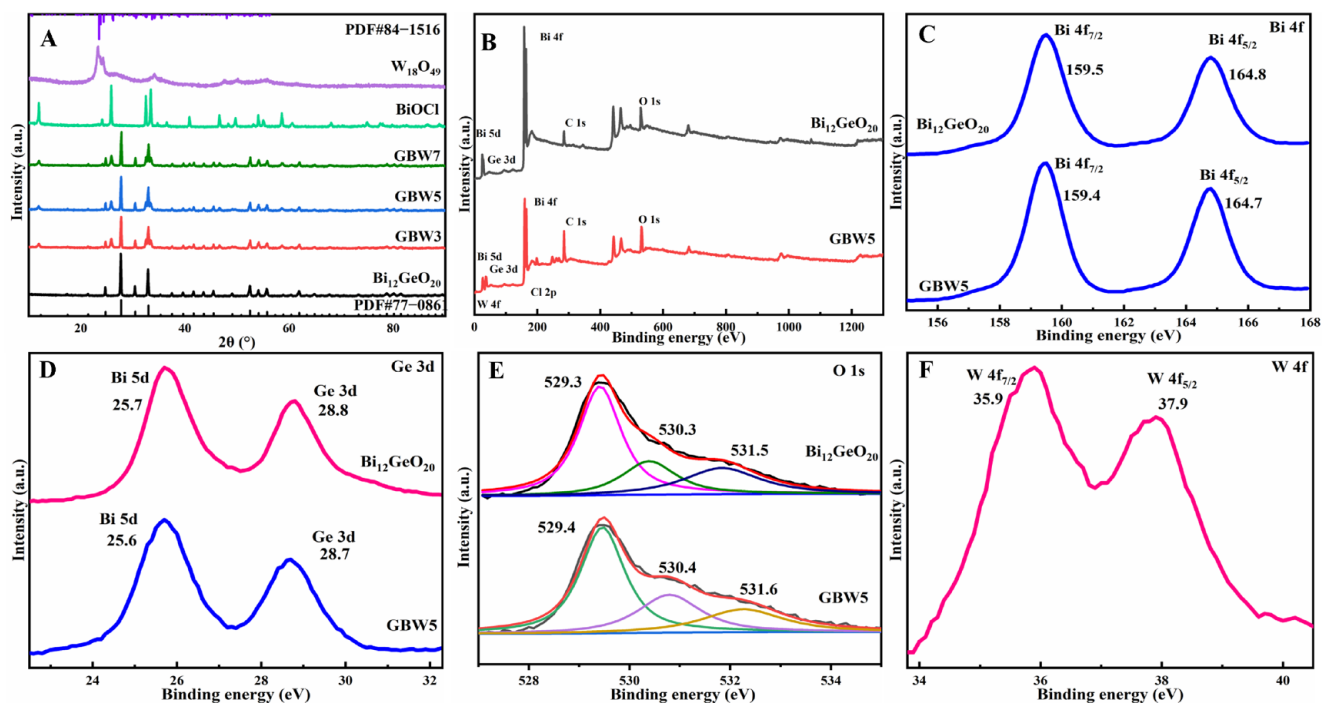


Figure 1. XRD patterns of $\text{Bi}_{12}\text{GeO}_{20}$, $\text{W}_{18}\text{O}_{49}$, and GBW composites (A), the full-scan XPS (B) and HR spectra of Bi 4f (C), Ge 3d (D), and O 1s (E) of $\text{Bi}_{12}\text{GeO}_{20}$ and GBW5, and HR spectrum of W 4f (F) of GBW5.

The chemical composition and surface valence states of $\text{Bi}_{12}\text{GeO}_{20}$ and composite GBW5 were analyzed using X-ray photoelectron spectroscopy (XPS). The full-scan spectrum

in Figure 1B confirms the presence of Bi, Ge, and O in both samples. In addition, the spectrum of GBW5 shows a distinct signal for W, with an atomic percentage of tungsten measured at 5.3%, which is consistent with the theoretical value of 5%. This confirms the successful incorporation of tungsten into the composites. To further distinguish the valence states of each element, high-resolution (HR) XPS spectra of Bi 4f, Ge 3d, O 1s, W 4f, and Cl 2p are exhibited in Figure 1C–F and Figure S3. In Figure 1C, the peaks at 159.5 and 164.8 eV in $\text{Bi}_{12}\text{GeO}_{20}$ and 159.4 and 164.7 eV in composite GBW5, respectively, correspond to the Bi 4f_{7/2} and Bi 4f_{5/2} orbitals [42]. The Bi 5d and Ge 3d signals at 25.7 and 28.8 eV in $\text{Bi}_{12}\text{GeO}_{20}$ can be seen in Figure 1D, and slightly shift to 25.6 eV and 28.7 eV in composite GBW5, confirming the presence of Bi³⁺ and Ge⁴⁺ cations in both samples. As to the O 1s spectra in Figure 1E, signals positioned at 529.3, 530.3 eV, and 531.5 eV in $\text{Bi}_{12}\text{GeO}_{20}$ respectively attribute to Ge–O bonds, Bi–O bonds, and adsorbed surface oxygen species. In addition, Figure 1F displays characteristic signals at 35.9 and 37.9 eV that correspond to the W 4f_{7/2} and W 4f_{5/2} orbitals, respectively. Figure S3 shows the characteristic signals at 198.2 and 199.7 eV, corresponding to the Cl 2p_{3/2} and Cl 2p_{1/2} orbitals, respectively. Compared with $\text{Bi}_{12}\text{GeO}_{20}$, the signal peaks of Bi 4f and Ge 3d in the GBW5 composite have shifted downfield, indicating a certain degree of electron transfer and migration to $\text{Bi}_{12}\text{GeO}_{20}$ [43], which further benefits the photocatalytic processes [44].

The microstructures and morphologies of $\text{Bi}_{12}\text{GeO}_{20}$, $\text{W}_{18}\text{O}_{49}$, and composite GBW5 were thoroughly examined using scanning electron microscopy (SEM) and transmission electron microscopy (TEM). The tetragonal-phased $\text{Bi}_{12}\text{GeO}_{20}$ exhibits an accumulation of regular large and incomplete small triangular pyramids of several micrometers in Figure 2A and Figure S4A. As shown in Figure 2B and Figure S4B, the $\text{W}_{18}\text{O}_{49}$ presents sea urchin-like spheres that are accumulated by numerous nanosheets. The composite GBW5 shows the morphology of nanosheets from sea urchin-like spheres covering the surface of triangular pyramids in Figure 2C and Figure S4C, which reveals the coexistence of both $\text{Bi}_{12}\text{GeO}_{20}$ and $\text{W}_{18}\text{O}_{49}$ components and facilitates reflection of incident light and mass transfer of reactants and products, thus improving photocatalytic outcomes. Unfortunately, it is difficult to see any BiOCl, which generally presents as lamellar structures, similar to that of $\text{W}_{18}\text{O}_{49}$. To this end, the elemental distribution of composite GBW5 was measured at the selected area in Figure S4D and the presence of Bi, Ge, O, W, and Cl is obviously confirmed in Figure S4E–I, corroborating the successful generation of ternary heterojunction composites. Furthermore, the SEM image of composite GB5 in Figure 2D and Figure S4J shows triangular pyramids with a rough surface and some small flakes adhered to them, in contrast to that of $\text{Bi}_{12}\text{GeO}_{20}$. The produced BiOCl phase exists as small flakes or particles closely attached to the surface of the $\text{Bi}_{12}\text{GeO}_{20}$, which can be identified from the elemental mapping images shown in Figure S4K–O. TEM and HRTEM images were employed to further investigate the morphologies and microstructures of relevant samples. The TEM image of composite GBW5 in Figure 2E reveals a sea urchin-like morphology including a bulky structure covered with numerous nanosheets, which is in good accordance with the SEM image in Figure 2C. In addition, some small particles attached to the surface among the nanosheets are observed. This area is framed by a red elliptical ring and was the target for high-resolution TEM analysis. Significantly, three kinds of well-defined lattice fringes are observable in Figure 2F. Lattice fringes in the bulky phase with a lattice spacing of approximately 0.27 nm correspond to the (321) crystal planes of $\text{Bi}_{12}\text{GeO}_{20}$. In addition, lattice fringes on nanosheets with lattice spacing of approximately 0.37 nm belong to the (010) crystal planes of $\text{W}_{18}\text{O}_{49}$, and other lattice fringes with lattice spacing of 0.32 nm belong to (110) crystal planes of BiOCl. This close contact of three kinds of components indicates the formation of the target composites, which can steer and redistribute charge carriers to promote photocatalytic reactions [45].

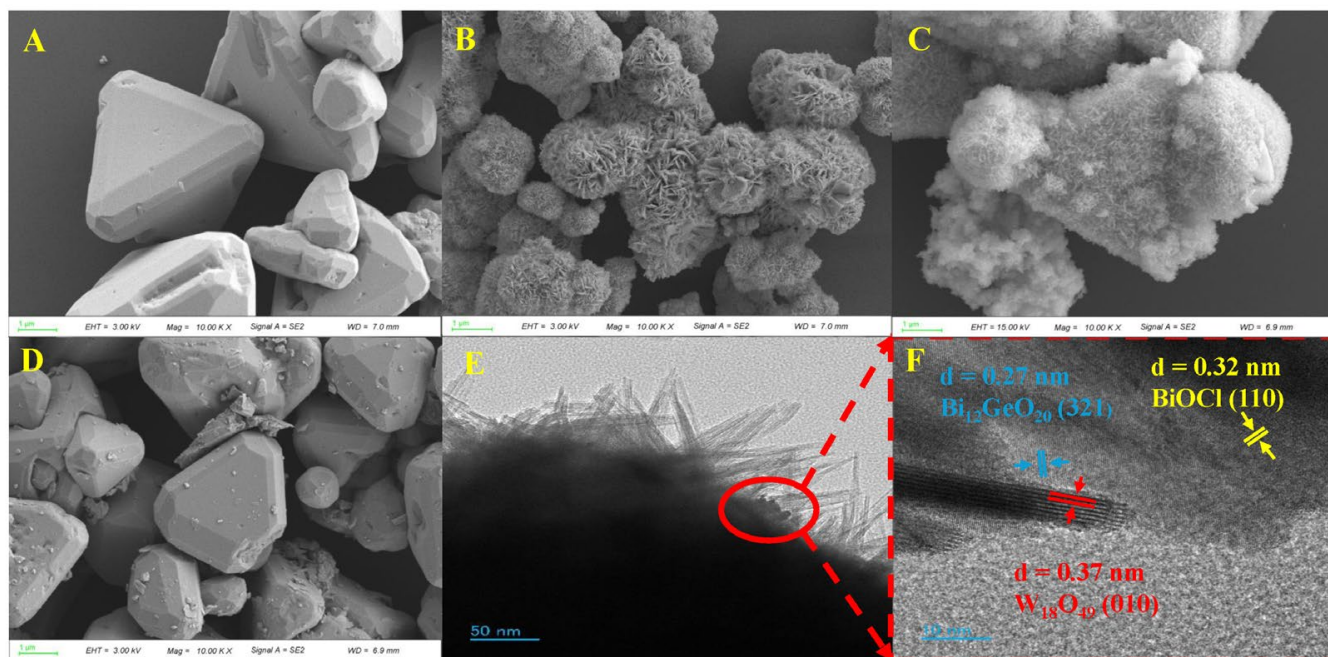


Figure 2. SEM images of $\text{Bi}_{12}\text{GeO}_{20}$ (A), $\text{W}_{18}\text{O}_{49}$ (B), composite GBW5 (C), and GB5 (D); TEM (E) and HRTEM (F) images of GBW5.

Ultraviolet–visible diffuse reflectance spectroscopy (UV–Vis DRS) was utilized to assess the optical properties and bandgap structures of the semiconductors. BiOCl in white shows strong adsorption in the ultraviolet region because of the wide bandgap shown in Figure 3A. Pristine $\text{Bi}_{12}\text{GeO}_{20}$ in light yellow exhibits an intensive absorption ranging from 200 to 500 nm, indicating a moderate response in the visible region. However, $\text{W}_{18}\text{O}_{49}$ in navy blue demonstrates a significant absorption in both the ultraviolet and visible regions, mainly owing to the suitable band structure with the localized surface plasmon resonance effect. As the $\text{W}_{18}\text{O}_{49}$ content of the composites increases, the absorption edge of the GBW composite progressively shifts toward shorter wavelengths, which is primarily attributed to the formation of heterojunction structures. From Figure 3A, the adsorption in the near-infrared region of composites is unable to induce variations in the photocatalytic performance, mainly due to insufficient incident energy. Instead, other effects, such as the dosage of the introduced catalyst [46], greatly affect photocatalytic outcomes. Figure S5 shows the UV–Vis DRS spectra of composites synthesized using NaCl as the chlorine source. Significantly, the absorption edge of these composites remains almost unchanged.

According to the calculations in Figure S6A–C, it was found that $\text{Bi}_{12}\text{GeO}_{20}$, $\text{W}_{18}\text{O}_{49}$, and BiOCl follow an indirect transition, with the value n as 4. The bandgap (E_g) of semiconductor-based samples can be computed from the equation $\alpha h\nu = A(h\nu - E_g)^{n/2}$, where α , A , h , and ν represent the absorption coefficient, a constant, Planck’s constant, and optical frequency, respectively. As shown in Figure 3B,C, the values of E_g of $\text{Bi}_{12}\text{GeO}_{20}$, $\text{W}_{18}\text{O}_{49}$, and BiOCl are determined to be 2.70, 2.76, and 3.26 eV, respectively. In Figure S7, the $(\alpha h\nu)^{1/2}$ vs $h\nu$ plots for the GBW series of samples reveal that the values of E_g gradually increase with increasing $\text{W}_{18}\text{O}_{49}$ content. Accordingly, the value of E_g of composite GBW5 is measured at 2.79 eV. It is well known that E_g refers to the energy required to excite electrons from the valence band (VB) to the conduction band (CB) in a semiconductor. The reduction in E_g in composite GBW5 facilitates visible light absorption, the generation of charge carriers, and further photocatalytic reactions.

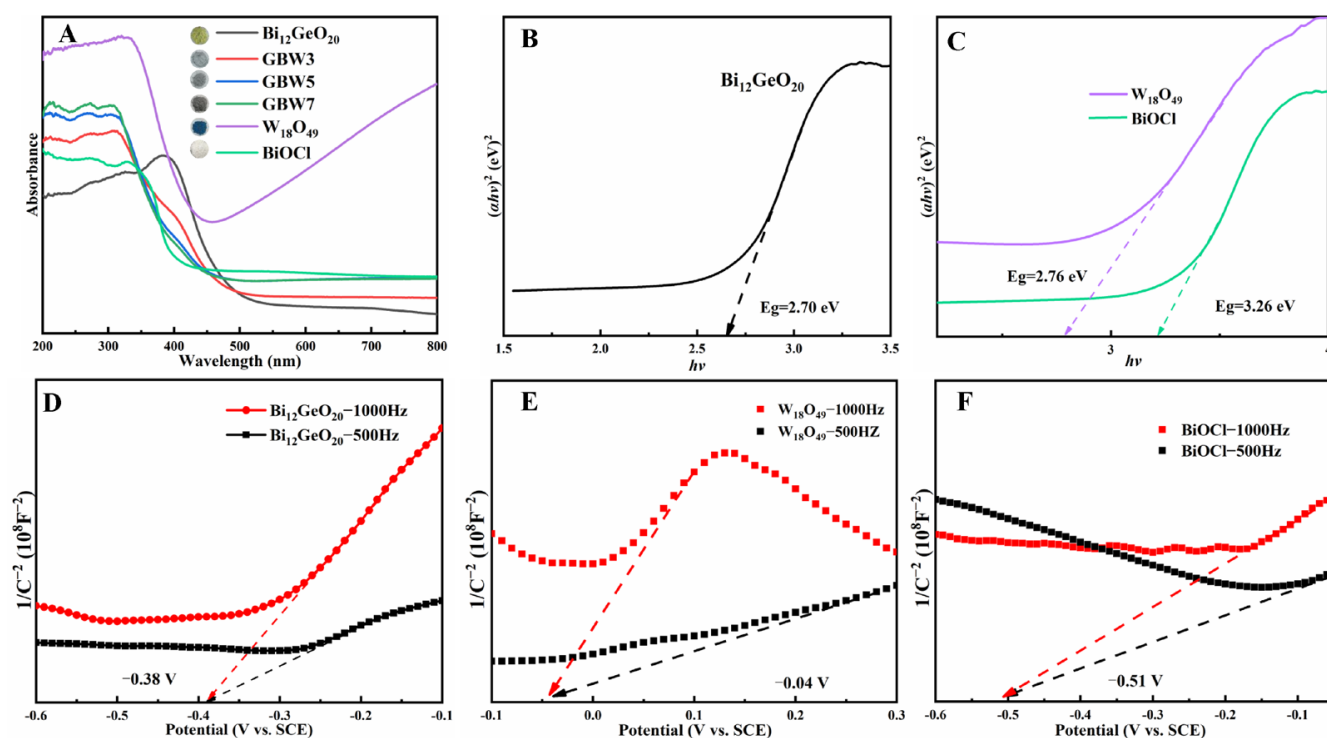


Figure 3. UV–Vis DRS spectra of $\text{Bi}_{12}\text{GeO}_{20}$, $\text{W}_{18}\text{O}_{49}$, BiOCl and GBW series with color in inset (A), E_g estimation of $\text{Bi}_{12}\text{GeO}_{20}$ (B), and $\text{W}_{18}\text{O}_{49}$ and BiOCl (C), Mott–Schottky plots of $\text{Bi}_{12}\text{GeO}_{20}$ (D), $\text{W}_{18}\text{O}_{49}$ (E) and BiOCl (F) measured at different frequencies.

The band structures of $\text{Bi}_{12}\text{GeO}_{20}$, $\text{W}_{18}\text{O}_{49}$, and BiOCl were inferred through flat-band potentials (E_{fb}) on an electrochemical workstation. The Mott–Schottky plots of $\text{Bi}_{12}\text{GeO}_{20}$, $\text{W}_{18}\text{O}_{49}$, and BiOCl are shown in Figure 3D–F, respectively. Usually, the type of semiconductor can be determined by analyzing the slope of the straight-line section, with a negative or positive slope indicating p-type or n-type characteristics, respectively. Clearly, the positive slopes in the linear regions in three samples suggest an n-type nature, and the slopes of $\text{Bi}_{12}\text{GeO}_{20}$ and BiOCl are smaller than that of $\text{W}_{18}\text{O}_{49}$, revealing the large charge carrier concentration and better photocatalytic performance [47]. The intersections with the x-axis and the straight-line section can allow values of E_{fb} for $\text{Bi}_{12}\text{GeO}_{20}$, $\text{W}_{18}\text{O}_{49}$, and BiOCl to be approximated as -0.38 , -0.04 , and -0.51 V (vs. saturated calomel electrode, SCE), respectively. By using the correction of 0.24 V, E_{fb} values are calculated as -0.14 , 0.20 , and -0.27 V (vs. normal hydrogen electrode, NHE) for $\text{Bi}_{12}\text{GeO}_{20}$, $\text{W}_{18}\text{O}_{49}$, and BiOCl , respectively. According to the characteristics of n-type semiconductors, their potentials of conduction band bottom (E_{CB}) are generally about 0.1 – 0.3 V higher than E_{fb} values. Herein, a median value of 0.2 V is chosen for calculation, and resultant values of E_{CB} of -0.34 , 0 , and -0.47 V are calculated for $\text{Bi}_{12}\text{GeO}_{20}$, $\text{W}_{18}\text{O}_{49}$, and BiOCl , respectively. Considering E_g values for $\text{Bi}_{12}\text{GeO}_{20}$, $\text{W}_{18}\text{O}_{49}$, and BiOCl , the potentials of the valence band top (E_{VB}) can be calculated to be 2.36 , 2.76 , and 2.79 V, respectively, using the formula $E_{CB} = E_{VB} - E_g$ [48].

2.2. Photocatalytic NO Removal Performance

Photocatalytic NO removal efficiencies were measured by placing catalysts in a reactor with continuously flowing NO gas under UV–visible irradiation. To ensure the accuracy and reproducibility of results, each experiment was conducted at least three times in parallel to provide average data with error bars. Prior to the experiments, the effect of relative humidity in the reactor over NO removal was assessed in the presence of composite GBW5, as shown in Figure S8. Obviously, the NO removal efficiency at 50% relative humidity is

approximately 20% higher than those at 25% and 75% relative humidity. Accordingly, 50% relative humidity was chosen for subsequent experiments.

The photocatalytic performance on NO removal by $\text{Bi}_{12}\text{GeO}_{20}$, $\text{W}_{18}\text{O}_{49}$, and the GBW series is depicted in Figure 4A. Both $\text{Bi}_{12}\text{GeO}_{20}$ and BiOCl exhibit weak removal efficiencies of around 10% after 30 min of light exposure, while $\text{W}_{18}\text{O}_{49}$ exhibits negligible catalytic activity under identical conditions. As for the GBW composites, their removal efficiencies increase greatly and achieve peak values after 5 min. In addition, the peak values can be maintained for up to 30 min, revealing the satisfactory stability of catalytic capacity. Moreover, with increasing WCl_6 addition, the photocatalytic performance of the GBW series first increases and then reduces. As a result, the composite GBW5 with a suitable composition exhibits the best removal efficiency of around 42%, which is significantly higher than those of pure $\text{Bi}_{12}\text{GeO}_{20}$, $\text{W}_{18}\text{O}_{49}$, and BiOCl . The trend in photocatalytic removal of NO_x (including NO and NO_2) under UV–visible light for different samples shown in Figure S9A shows the same behavior as for the NO removal shown in Figure 4A. However, GBW composites cause a slight increase in NO_2 production in comparison to pure $\text{Bi}_{12}\text{GeO}_{20}$, $\text{W}_{18}\text{O}_{49}$, and BiOCl , as shown in Figure S9B, which is unexpected since NO_2 molecules are more toxic than NO. For a comprehensive evaluation of NO_x elimination, both the NO removal and NO_2 generation should be considered by using the DeNO_x index. The larger the DeNO_x index, the better the photocatalytic performance. Significantly, as shown in Figure 4B, the DeNO_x index of GBW5 is the largest among all values by the different candidates, revealing the best overall efficiency among all as-synthesized samples. In order to confirm the generation of nitrate (NO_3^-) and nitrite (NO_2^-) species during the photocatalytic processes, XPS spectra of composite GBW5 stirred for 1 h in an aqueous solution containing NaNO_3 and NaNO_2 and after five consecutive runs (150 min) were recorded. As shown in Figure S10, signals at 403.2 and 407.3 eV are both clearly visible in the spectra for GBW5 stirred for 1 h in an aqueous solution, assigned to NO_2^- and NO_3^- adsorbed on the surface, respectively. A distinct signal at 406.7 eV is observed in GBW5 after a reaction of 150 min, indicating the formation of NO_3^- species during the reaction. The absence of another signal indexed to NO_2^- is possibly attributed to its instability and ease of converting to stable NO_3^- . Generally, the apparent reaction kinetics constant (K_{app}) of catalyst processes can be calculated from the pseudo-first-order kinetic as shown in Figure S11 and Figure 4C. As can be seen, the composite GBW5 has the largest K_{app} value at $67.83 \times 10^{-3} \text{ min}^{-1}$, which is about 3.7 and 24 times those of $\text{Bi}_{12}\text{GeO}_{20}$ and $\text{W}_{18}\text{O}_{49}$, respectively. From the aforementioned experimental results, the GBW ternary heterojunction composites exhibit visibly improved photocatalytic capacity in comparison to the individual materials. As shown in Figure S12, the photocatalytic NO removal and NO_2 generation with the binary composites GB are slightly better than those with pure $\text{Bi}_{12}\text{GeO}_{20}$ and BiOCl but nowhere near as good as those with the GBW series, revealing the synergistic effect of integrating three components with the appropriate composition. On the whole, our catalyst system provides comparable and even better removal efficiencies in comparison to recent relevant reports, which are collected in Table S2 [49–56].

The transfer and segregation efficiency of photogenerated charge carriers can be assessed using electrochemical impedance spectroscopy (EIS) and transient photocurrent measurements, which directly relate to the photocatalytic performance of the catalysts. The EIS Nyquist plots demonstrate the interfacial impedance between electrode and electrolyte, where a smaller radius means a weaker charge transfer resistance. The Nyquist plots of $\text{Bi}_{12}\text{GeO}_{20}$, $\text{W}_{18}\text{O}_{49}$, BiOCl , and composite GBW5 are shown in Figure 4D. Clearly, the arc radii of relevant samples change in an order of $\text{GBW5} < \text{BiOCl} < \text{Bi}_{12}\text{GeO}_{20} < \text{W}_{18}\text{O}_{49}$ with the corresponding fitted data collected in Table S1, which is in good agreement with the trend in photocatalytic capacity. The intensity of the transient photocurrent indicates the

transfer rate of photogenerated carriers under illumination. As shown in Figure 4E, composite GBW5 demonstrates the highest steady-state photocurrent response, far exceeding those of other samples, revealing the highly efficient migration and segregation efficiency of ternary heterojunction systems arising from the integration of the structural merits of the three components.

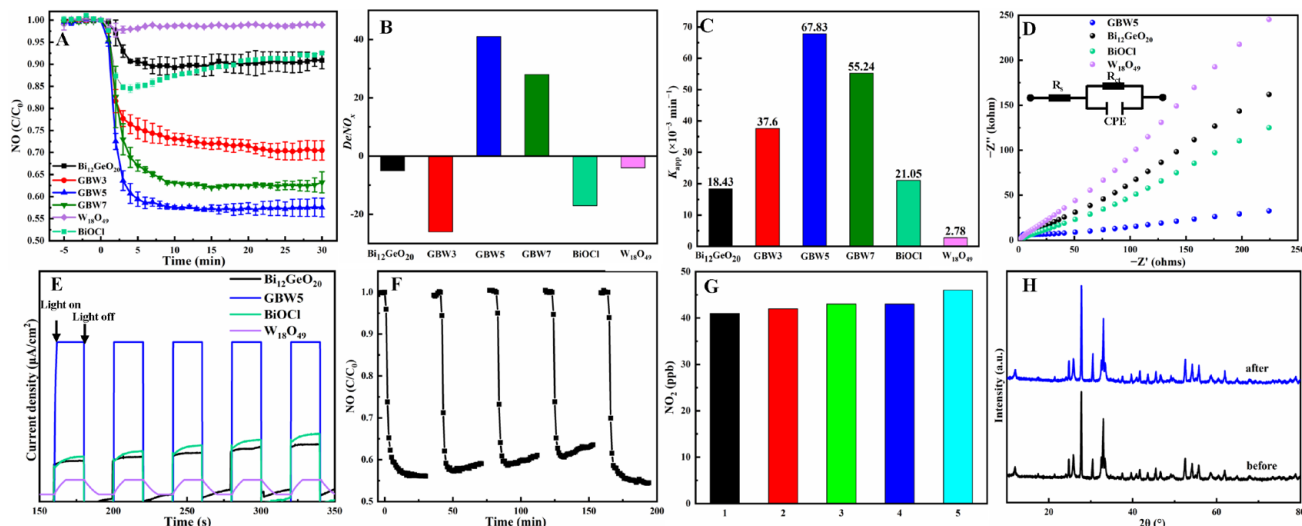


Figure 4. Photocatalytic NO removal under ultraviolet–visible light (A), DeNO_x indexes (B), and K_{app} values (C) by Bi₁₂GeO₂₀, W₁₈O₄₉, BiOCl, and GBW series, EIS spectra (D) and photocurrent transient responses (E) of relevant samples, photocatalytic NO removal (F) and generation of NO₂ (G) by GBW5 for five cycles, XRD patterns of GBW5 before and after five cycles (H).

Five repeated photocatalytic experiments were conducted to estimate the recycling capability and structural stability of the as-synthesized composites. The first four experiments were consecutively carried out without interruption, the used GBW5 was then washed three times each with water and ethanol before being subjected to the fifth cycle. As shown in Figure 4F, photocatalytic performance remains high with only a slight reduction after four cycles and can be restored in the fifth cycle after simply washing. During photocatalytic processes, NO₂ generation remains approximately invariant, as shown in Figure 4G. These results confirm the impressive reusability of the composite. In addition, the XRD patterns of GBW5 before and after five cycles are identical, suggesting good maintenance of the composite and crystal structure, which indicates the sufficient structural stability of these robust samples.

By conducting capture experiments, the reactive species that contribute to photocatalytic processes can be identified. As depicted in Figure 5A, the photocatalytic removal efficiency of GBW5 is greatly inhibited after the addition of reagents KI, PBQ, TBA, or K₂CrO₇, confirming the crucial roles of species h⁺, e⁻, ·O₂⁻, and ·OH. The generation of ·OH radicals can be directly detected by fluorescence spectroscopy (PL). After light exposure for 30 min, intensive bands centered at 425 nm appear, as shown in Figure 5B, verifying the formation of ·OH radicals in the presence of both Bi₁₂GeO₂₀ and GBW5. Moreover, the fluorescence signal intensity of GBW5 is higher than that of Bi₁₂GeO₂₀, indicating the boosted generation of ·OH radicals due to the strong oxidative capability of these ternary composites. To further detect the formation ·OH and ·O₂⁻ radicals, electron spin resonance (ESR) measurements were performed. The typical signals of DMPO·OH adducts in the spectra of both Bi₁₂GeO₂₀ and composite GBW5 are visible in Figure 5C. Neither Bi₁₂GeO₂₀ nor GBW5 causes the generation of ·OH radicals in the dark. In contrast, evident ESR signals in the spectra of both samples can be found after 10 min of light irradiation, revealing

the possible formation of $\cdot\text{OH}$ radicals upon illumination. Moreover, the stronger ESR signals generated with GBW5 compared to those generated with $\text{Bi}_{12}\text{GeO}_{20}$ suggest the strengthened production of $\cdot\text{OH}$ radicals because of efficient regulation of interfacial charge carriers in ternary composites. Similar results are found for the appearance of $\text{DMPO}\cdot\text{O}_2^-$ signals in methanol under light illumination in Figure 5D, revealing that more $\cdot\text{O}_2^-$ radicals can be produced by GBW5 than by $\text{Bi}_{12}\text{GeO}_{20}$. Although the GBW5 and $\text{Bi}_{12}\text{GeO}_{20}$ catalytic systems are both able to induce the production of $\cdot\text{OH}$ and $\cdot\text{O}_2^-$ radicals, the synergistic effect represented by the ternary composites is favorable for the formation of sufficient radicals, thus enhancing photocatalytic NO removal performance [48].

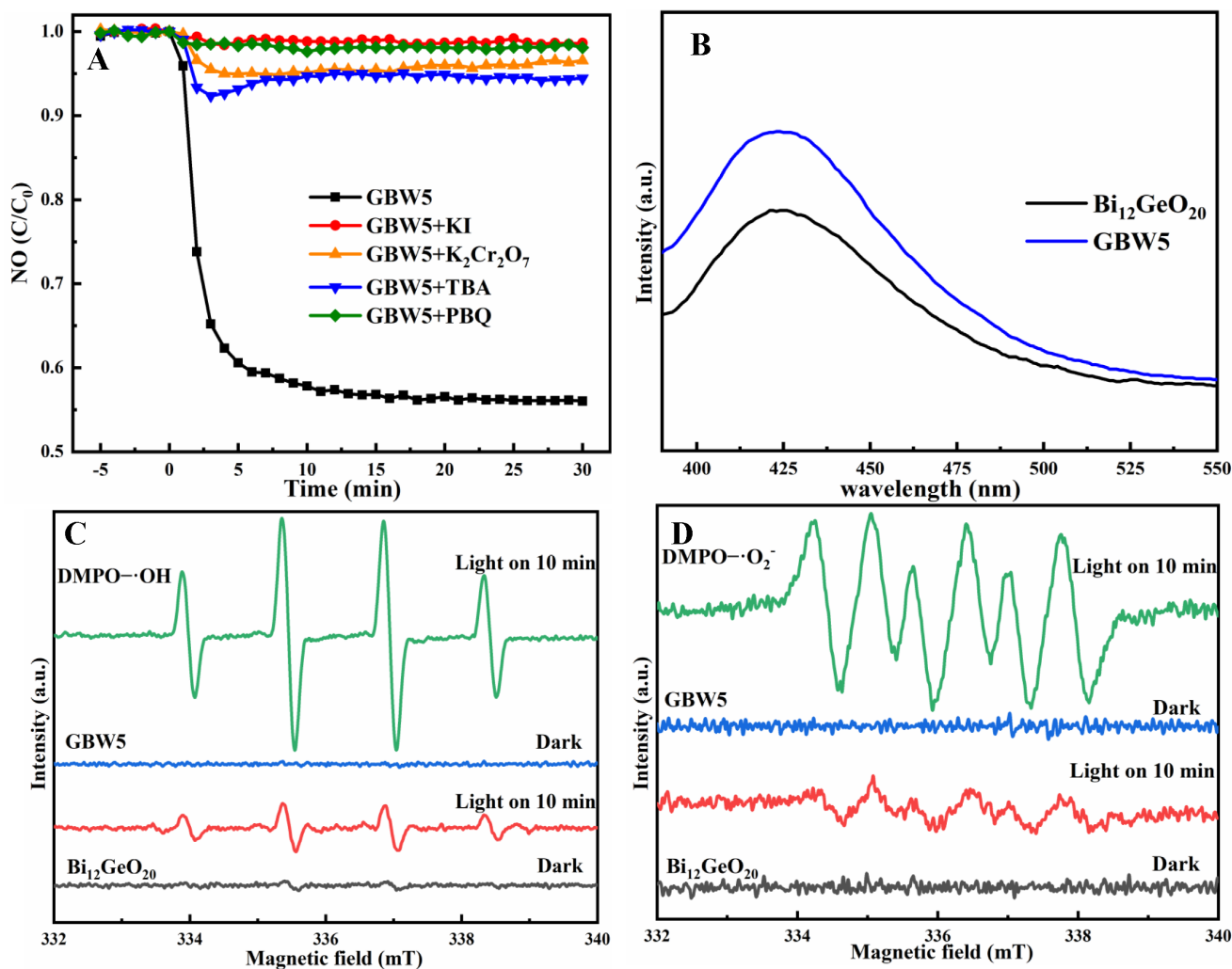


Figure 5. Photocatalytic NO removal by GBW5 in the presence of different capture reagents (A), PL spectra of $\text{Bi}_{12}\text{GeO}_{20}$ and GBW5 (B), ESR spectra of adducts $\text{DMPO}\cdot\text{OH}$ (C) and $\text{DMPO}\cdot\text{O}_2^-$ (D) of $\text{Bi}_{12}\text{GeO}_{20}$ and GBW5 in dark and under visible light at different time.

Based on the experimental and analytical results described above, a probable mechanism for photocatalytic NO removal using the GBW composites is proposed in Figure 6. As described, $\text{W}_{18}\text{O}_{49}$ and BiOCl phases are generated on the surface of $\text{Bi}_{12}\text{GeO}_{20}$, thus the relative position of the three components with relevant band structures is exhibited on the left side of the diagram. The production of a BiOCl phase on the surface of $\text{Bi}_{12}\text{GeO}_{20}$ through the comprehensive utilization of “waste” Cl anions may form a heterojunction structure that regulates interfacial charge carriers. In addition, the presence of $\text{W}_{18}\text{O}_{49}$ nanosheets is capable of enhancing visible light absorption and promoting the separation of charge carriers. As a result, a synergistic effect is formed at the interface between the

three components. Under ultraviolet–visible light, the three components are excited and distribute electrons to the CB and holes to the VB. BiOCl possesses a more negative CB and positive VB than $\text{Bi}_{12}\text{GeO}_{20}$, thus, electrons and holes from BiOCl tend to thermodynamically transfer to $\text{Bi}_{12}\text{GeO}_{20}$. Because of the faster transfer rate of e^- than h^+ , more electrons accumulate in the CB of $\text{Bi}_{12}\text{GeO}_{20}$ as revealed by XPS analyses and more holes remain in the VB of BiOCl, thus causing efficient segregation efficiency through a Type I scheme. Subsequently, holes in the VB of $\text{Bi}_{12}\text{GeO}_{20}$ can recombine with electrons on $\text{Bi}_{12}\text{GeO}_{20}$ and holes on $\text{W}_{18}\text{O}_{49}$ through a Z-scheme model. Accordingly, electrons easily convert to $\cdot\text{O}_2^-$ radical because of the more negative CB potential of $\text{Bi}_{12}\text{GeO}_{20}$ (0.34 V) than the potential ($\text{O}_2^- / \cdot\text{O}_2^-$, -0.33 V), and holes readily convert to $\cdot\text{OH}$ radicals because of more positive VB potentials of BiOCl (2.79 V) and $\text{W}_{18}\text{O}_{49}$ (2.76 V) than potentials ($\text{OH}^- / \cdot\text{OH}$, 1.99 V) and ($\text{H}_2\text{O} / \cdot\text{OH}$, 2.27 V), which can be confirmed by the entrapping experiments, PL spectra, and ESR spectra in Figure 5. As a result, the combination of both Type I and Z-scheme transfer models effectively suppresses the recombination of photogenerated charge carriers, prolongs the lifetimes of charge carriers, and enhances the light-responsive capability, thus facilitating the improvement of photocatalytic NO removal efficiencies of the GBW ternary heterojunction composites.

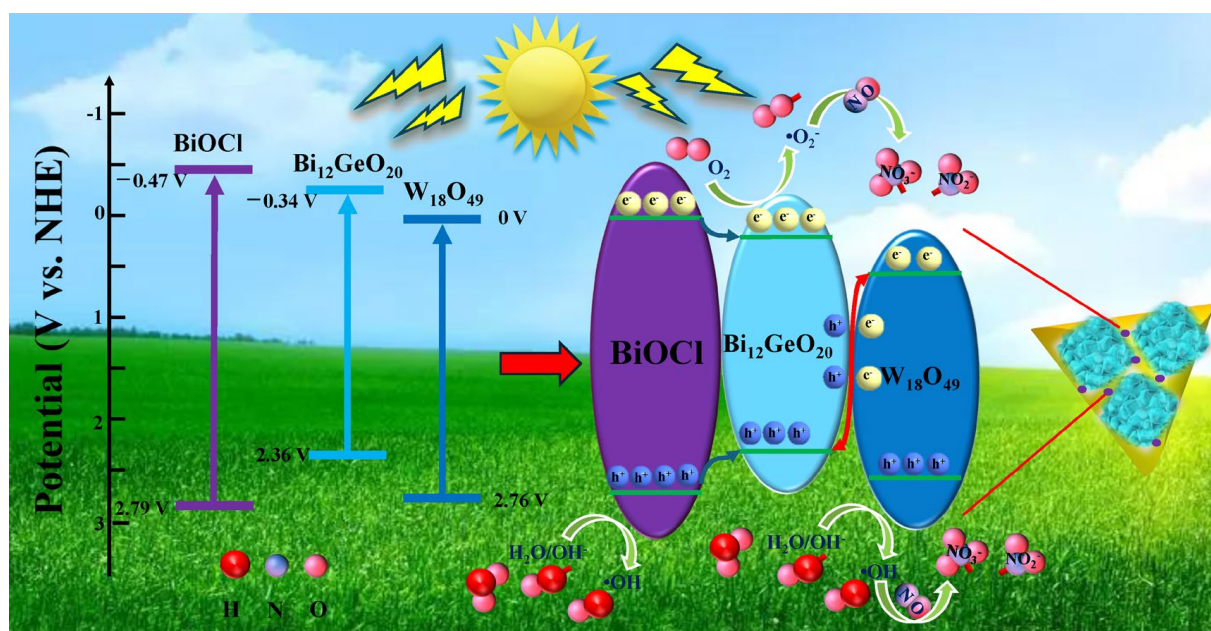


Figure 6. The mechanism diagram of photocatalytic NO removal by GBW composites.

3. Materials and Methods

3.1. Catalysts Fabrication

Detailed information on the reagents used in this study can be found in the Supplementary Materials. The original $\text{Bi}_{12}\text{GeO}_{20}$ was simply prepared by a solvothermal method. Typically, $\text{Bi}(\text{NO}_3)_3 \cdot 5\text{H}_2\text{O}$ (2.91 g, 6 mmol) was dispersed in a NaOH solution (5 M, 35 mL), and the mixture was stirred magnetically until the color turned to light yellow. Subsequently, GeO_2 (0.05 g, 0.5 mmol) and cetyltrimethylammonium bromide (0.25 g, 0.7 mmol) were added to the solution to make a mixture that was vigorously stirred for 30 min. The resultant mixture was then transferred to a Teflon-lined autoclave. After heating at 180°C for 12 h, the suspension was centrifuged, washed three times with water and ethanol, and then dried at 60°C for 8 h to obtain pristine $\text{Bi}_{12}\text{GeO}_{20}$. $\text{W}_{18}\text{O}_{49}$ was synthesized using WCl_6 as the tungsten source and anhydrous ethanol as the solvent through a solvothermal method [33].

The ternary composites were fabricated by a post-synthesis protocol, where the as-synthesized $\text{Bi}_{12}\text{GeO}_{20}$ was added during the preparation of $\text{W}_{18}\text{O}_{49}$. Typically, the required amount of WCl_6 (0.065 g, 0.108 g, 0.151 g) was dissolved in anhydrous ethanol (40 mL) to produce a mixture that was stirred until the yellow solution turned colorless. Afterward, $\text{Bi}_{12}\text{GeO}_{20}$ (1 g) was added and the resultant suspension was magnetically stirred for 30 min, followed by ultrasonic treatment for another 30 min. The mixture was then transferred to a Teflon-lined autoclave and heated at 160 °C for 12 h. After cooling to room temperature, the precipitate was collected by centrifugation, washed three times with water and alcohol, and dried in a vacuum oven at 60 °C for 6 h. These obtained composites were labeled GBW3, GBW5, and GBW7 according to the mass ratio of elemental W to $\text{Bi}_{12}\text{GeO}_{20}$. During the aforementioned procedure, BiOCl was also synthesized by a solvothermal method as follows. $\text{Bi}(\text{NO}_3)_3 \cdot 5\text{H}_2\text{O}$ (0.97 g, 2 mmol) in ethylene glycol (76 mL) and NaCl (0.234 g, 4 mmol) in water (5 mL) were mixed to gain a mixture that was stirred for 30 min and then left to stand at 140 °C for 5 h to supply BiOCl . Binary composites $\text{Bi}_{12}\text{GeO}_{20}/\text{BiOCl}$ were synthesized using a similar procedure to that of the ternary composites, except that WCl_6 was replaced by NaCl as the chlorine source, based on moles of Cl element. The synthesized composites were labeled GB3, GB5, and GB7. The schematic diagram of the synthetic procedure of the as-synthesized samples is shown in Figure S1.

The microstructural analyses and relevant instruments are listed in the Supplementary Materials for clarity.

3.2. Photocatalytic NO Removal and Entrapping Experiments

The specific procedure for the photocatalytic NO removal and recycling experiments are provided in the Supplementary Materials. Entrapping experiments were conducted to identify the reactive species that played roles during photocatalytic NO removal. To that end, a reagent such as KI (0.1 g), tert-butanol (TBA, 0.1 mM), p-benzoquinone (PBQ, 0.1 g), or potassium dichromate (K_2CrO_7 , 0.1 g) was introduced into the photocatalytic systems to trap holes (h^+), hydroxyl radicals ($\cdot\text{OH}$), superoxide radicals ($\cdot\text{O}_2^-$), or e^- , respectively. The procedure was the same as that used for photocatalytic NO removal. The active species $\cdot\text{OH}$ and $\cdot\text{O}_2^-$ captured by 5,5-dimethyl-1-pyrroline N-oxide (DMPO) and 2,2,6,6-tetramethyl-4-piperidone hydrochloride (TEMP) were detected using electron spin resonance (ESR) spectroscopy. $\cdot\text{OH}$ radicals entrapped by terephthalic acid were detected using an F96Pro spectrophotometer (Shanghai Lengguang Technology Co., Ltd., Shanghai, China).

4. Conclusions

In this investigation, the integration of “sea urchin-like” $\text{W}_{18}\text{O}_{49}$ and BiOCl by comprehensively utilizing all ions in precursor WCl_6 was successfully completed on the surface of $\text{Bi}_{12}\text{GeO}_{20}$, leading to the generation of ternary composites, designated GBW. These as-prepared composites were thoroughly analyzed by various techniques and subjected to photocatalytic NO removal evaluation. Consistent with expectations, these ternary composites showed enhanced photocatalytic performance under UV–visible irradiation. Among all tested samples, the composite GBW5 showed the highest NO photocatalytic removal efficiency of 42%, which was nearly four times that of pure $\text{Bi}_{12}\text{GeO}_{20}$. In addition, it possessed the largest K_{app} value and DeNO_x index, which was mainly attributed to enhanced light absorption, suitable morphological features, effective separation of charge carriers, and boosted generation of reactive species. Based on the analytical and experimental results, the robust GBW composites underwent a combination of both Type I and Z-scheme transfer, by which charge carriers could efficiently migrate and be segregated. This study paves the way for the construction of $\text{Bi}_{12}\text{GeO}_{20}$ -based ternary composites using

a comprehensive utilization of waste matter and their employment for the photocatalytic removal of low concentrations of NO at the ppb level.

Supplementary Materials: The following supporting information can be downloaded at: <https://www.mdpi.com/article/10.3390/catal15010073/s1>, Figure S1: Graphical illustration of synthetic procedure for target composites; Figure S2: XRD patterns of Bi₁₂GeO₂₀, BiOCl, and the GB series; Figure S3: XPS spectrum of Cl 2p in GBW5; Figure S4: SEM images of Bi₁₂GeO₂₀ (A), W₁₈O₄₉ (B), and GBW5 (C); EDS elemental mapping of total (D), and Bi (E), Ge (F), O (G), W (H), and Cl (I) elements; SEM images of GB5 (J) and EDS elemental mapping of GB5 (L–O) from the selected area in SEM image of GB5 (K); Figure S5: UV–visible DRS spectra of Bi₁₂GeO₂₀ and GB series; Figure S6: Estimation of n for Bi₁₂GeO₂₀ (A), W₁₈O₄₉ (B), and BiOCl (C); Figure S7: Estimation of E_g for GBW series; Figure S8: Photocatalytic NO removal by GBW5 at different relative humidities; Figure S9: Photocatalytic NO_x removal (A) and NO₂ production (B) by various samples; Figure S10: Corresponding pseudo-first-order curves of various samples; Figure S10: XPS spectra of composite GBW5 treated with a solution containing NO₂[−] and NO₃[−] anions and after five photocatalytic runs; Figure S11: Corresponding pseudo-first-order curves of various samples; Figure S12: Photocatalytic NO removal (A) and NO₂ production efficiency (B) by Bi₁₂GeO₂₀, BiOCl, and GB series; Table S1: Correlation fitting parameters of EIS spectra of Bi₁₂GeO₂₀, W₁₈O₄₉, BiOCl, and GBW5; Table S2: Comparison of photocatalytic performance of previous reports and our work. References [49–56] are cited in the supplementary materials.

Author Contributions: Supervision and funding acquisition, F.C.; Writing—original draft preparation and Investigation, W.B.; Investigation, J.L.; Investigation, Z.Z.; Writing—review and editing, D.L. All authors have read and agreed to the published version of the manuscript.

Funding: This research was funded by the Shanghai Municipal Natural Science Foundation, grant number 17ZR1419200. This research has also received financial support from the National Key Research and Development Program of China, grant number 2024YFE0211700.

Data Availability Statement: Dataset available on request from the authors.

Conflicts of Interest: The authors declare no conflicts of interest.

References

1. Li, N.; Wang, C.; Zhang, K.; Lv, H.; Yuan, M.; Bahnemann, D.W. Progress and Prospects of Photocatalytic Conversion of Low-Concentration NO. *Chin. J. Catal.* **2022**, *43*, 2363–2387. [[CrossRef](#)]
2. Lu, Y.; Chen, M.; Jiang, L.; Cao, J.; Li, H.; Lee, S.C.; Huang, Y. Oxygen Vacancy Engineering of Photocatalytic Nanomaterials for Enrichment, Activation, and Efficient Removal of Nitrogen Oxides with High Selectivity: A Review. *Environ. Chem. Lett.* **2022**, *20*, 3905–3925. [[CrossRef](#)]
3. Ma, C.; Wei, J.; Jiang, K.; Chen, J.; Yang, Z.; Yang, X.; Yu, G.; Zhang, C.; Li, X. Typical Layered Structure Bismuth-Based Photocatalysts for Photocatalytic Nitrogen Oxides Oxidation. *Sci. Total Environ.* **2023**, *855*, 158644. [[CrossRef](#)] [[PubMed](#)]
4. Lelieveld, J.; Pöschl, U. Chemists Can Help to Solve the Air-Pollution Health Crisis. *Nature* **2017**, *551*, 291–293. [[CrossRef](#)]
5. Pan, Y.; Wang, Y.; Zhang, J.; Liu, Z.; Wang, L.; Tian, S.; Tang, G.; Gao, W.; Ji, D.; Song, T.; et al. Redefining the Importance of Nitrate during Haze Pollution to Help Optimize an Emission Control Strategy. *Atmos. Environ.* **2016**, *141*, 197–202. [[CrossRef](#)]
6. Binas, V.; Venieri, D.; Kotzias, D.; Kiriakidis, G. Modified TiO₂ Based Photocatalysts for Improved Air and Health Quality. *J. Mater.* **2017**, *3*, 3–16. [[CrossRef](#)]
7. Serpone, N. Heterogeneous Photocatalysis and Prospects of TiO₂-Based Photocatalytic DeNO_xing the Atmospheric Environment. *Catalysts* **2018**, *8*, 553. [[CrossRef](#)]
8. Deorsola, F.A.; Andreoli, S.; Armandi, M.; Bonelli, B.; Pirone, R. Unsupported Nanostructured Mn Oxides Obtained by Solution Combustion Synthesis: Textural and Surface Properties, and Catalytic Performance in NO_x SCR at Low Temperature. *Appl. Catal. A Gen.* **2016**, *522*, 120–129. [[CrossRef](#)]
9. Guo, M.-Z.; Ling, T.-C.; Poon, C.S. Highly-Efficient Green Photocatalytic Cementitious Materials with Robust Weathering Resistance: From Laboratory to Application. *Environ. Pollut.* **2021**, *273*, 116510. [[CrossRef](#)]
10. Hu, W.; Gao, X.; Deng, Y.; Qu, R.; Zheng, C.; Zhu, X.; Cen, K. Deactivation Mechanism of Arsenic and Resistance Effect of SO₄^{2−} on Commercial Catalysts for Selective Catalytic Reduction of NO with NH₃. *Chem. Eng. J.* **2016**, *293*, 118–128. [[CrossRef](#)]

11. Gao, M.; Hu, X.; Wang, C.; Fei, Y.; Li, Z.; Xie, H.; Yang, M. Iron Mediated $n \rightarrow \pi^*$ Electron Transitions and Mid-Gap States Formation in CN under Low-Temperature Secondary Calcination Enhances Photodegradation of Organic Pollutants. *Sep. Purif. Technol.* **2025**, *357*, 130223. [[CrossRef](#)]
12. Dong, X.; Cui, W.; Wang, H.; Li, J.; Sun, Y.; Wang, H.; Zhang, Y.; Huang, H.; Dong, F. Promoting Ring-Opening Efficiency for Suppressing Toxic Intermediates during Photocatalytic Toluene Degradation via Surface Oxygen Vacancies. *Sci. Bull.* **2019**, *64*, 669–678. [[CrossRef](#)] [[PubMed](#)]
13. Bai, Y.; Hu, X.; Tian, T.; Cai, B.; Li, Y. Carbon Pre-Protected Iron Strategy to Construct Fe, C-Codoped g-C₃N₄ for Effective Photodegradation of Organic Pollutants via Hole Oxidation Mechanism. *J. Clean. Prod.* **2024**, *437*, 140739. [[CrossRef](#)]
14. Fragoso, J.; Barreca, D.; Bigiani, L.; Gasparotto, A.; Sada, C.; Lebedev, O.I.; Modin, E.; Pavlovic, I.; Sánchez, L.; Maccato, C. Enhanced Photocatalytic Removal of NO_x Gases by β -Fe₂O₃/CuO and β -Fe₂O₃/WO₃ Nanoheterostructures. *Chem. Eng. J.* **2022**, *430*, 132757. [[CrossRef](#)]
15. Li, K.; Zhou, W.; Li, X.; Li, Q.; Carabineiro, S.A.C.; Zhang, S.; Fan, J.; Lv, K. Synergistic Effect of Cyano Defects and CaCO₃ in Graphitic Carbon Nitride Nanosheets for Efficient Visible-Light-Driven Photocatalytic NO Removal. *J. Hazard. Mater.* **2023**, *442*, 130040. [[CrossRef](#)]
16. Maggos, T.; Bartzis, J.G.; Leva, P.; Kotzias, D. Application of Photocatalytic Technology for NO_x Removal. *Appl. Phys. A* **2007**, *89*, 81–84. [[CrossRef](#)]
17. Wang, H.; Sun, Y.; Jiang, G.; Zhang, Y.; Huang, H.; Wu, Z.; Lee, S.C.; Dong, F. Unraveling the Mechanisms of Visible Light Photocatalytic NO Purification on Earth-Abundant Insulator-Based Core–Shell Heterojunctions. *Environ. Sci. Technol.* **2018**, *52*, 1479–1487. [[CrossRef](#)]
18. Lasek, J.; Yu, Y.-H.; Wu, J.C.S. Removal of NO_x by Photocatalytic Processes. *J. Photochem. Photobiol. C Photochem. Rev.* **2013**, *14*, 29–52. [[CrossRef](#)]
19. Leson, G.; Winer, A.M. Biofiltration: An Innovative Air Pollution Control Technology For VOC Emissions. *J. Air Waste Manag. Assoc.* **1991**, *41*, 1045–1054. [[CrossRef](#)]
20. Popp, D. International Innovation and Diffusion of Air Pollution Control Technologies: The Effects of NO_x and SO₂ Regulation in the US, Japan, and Germany. *J. Environ. Econ. Manag.* **2006**, *51*, 46–71. [[CrossRef](#)]
21. Rao, F.; An, Y.; Huang, X.; Zhu, L.; Gong, S.; Shi, X.; Lu, J.; Gao, J.; Huang, Y.; Wang, Q.; et al. “X-Scheme” Charge Separation Induced by Asymmetrical Localized Electronic Band Structures at the Ceria Oxide Facet Junction. *ACS Catal.* **2023**, *13*, 2523–2533. [[CrossRef](#)]
22. Wang, H.; Li, K.; Li, J.; Sun, Y.; Dong, F. Photochemical Transformation Pathways of Nitrates from Photocatalytic NO_x Oxidation: Implications for Controlling Secondary Pollutants. *Environ. Sci. Technol. Lett.* **2021**, *8*, 873–877. [[CrossRef](#)]
23. Kuppusamy, M.; Kim, S.-W.; Lee, K.-P.; Jo, Y.J.; Kim, W.-J. Development of TiO₂–CaCO₃ Based Composites as an Affordable Building Material for the Photocatalytic Abatement of Hazardous NO_x from the Environment. *Nanomaterials* **2024**, *14*, 136. [[CrossRef](#)]
24. Kuppusamy, M.; Passi, M.; Sundaram, S.K.; Vadivel, G.; Rathinasamy, M.; Lee, K.-P.; Kim, W.-J. Synergistic Effect of Li, La Co-Doping on Photocatalytic Activity of BaTiO₃ Ferroelectric Material for Effective Degradation of Toxic NO_x for Environmental Remediation. *J. Environ. Chem. Eng.* **2024**, *12*, 112801. [[CrossRef](#)]
25. Cremades, A.; Santos, M.T.; Remón, A.; García, J.A.; Diéguez, E.; Piqueras, J. Cathodoluminescence and Photoluminescence in the Core Region of Bi₁₂GeO₂₀ and Bi₁₂SiO₂₀ Crystals. *J. Appl. Phys.* **1996**, *79*, 7186–7190. [[CrossRef](#)]
26. De Mello, A.C.S.; Santana, G.C.; Jackson, R.A.; Macedo, Z.S.; Moreira, S.G.C.; Valerio, M.E.G. Optical Properties of Pure and Cr³⁺ Doped BGO Ceramic Scintillators. *Phys. Status Solidi (c)* **2007**, *4*, 980–983. [[CrossRef](#)]
27. Moraes, C.G.P.; Jesus, F.A.A.; Macedo, Z.S. Electrical and Dielectric Characterization of Bi₁₂GeO₂₀ Prepared by Modified Pechini Method. *Adv. Condens. Matter Phys.* **2014**, *2014*, 968349. [[CrossRef](#)]
28. Wan, Z.; Zhang, G. Controlled Synthesis and Visible Light Photocatalytic Activity of Bi₁₂GeO₂₀ Uniform Microcrystals. *Sci. Rep.* **2014**, *4*, 6298. [[CrossRef](#)]
29. Chen, Y.; Fang, J.; Lu, S.; Cen, C.; Cheng, C.; Ren, L.; Feng, W.; Fang, Z. Hydrothermal Synthesis of a Ba and Mg Co-Doped Bi₁₂GeO₂₀ Photocatalyst with Enhanced Visible Light Catalytic Activity. *RSC Adv.* **2016**, *6*, 15745–15752. [[CrossRef](#)]
30. Wan, Z.; Zhang, G.; Wu, X.; Yin, S. Novel Visible-Light-Driven Z-Scheme Bi₁₂GeO₂₀/g-C₃N₄ Photocatalyst: Oxygen-Induced Pathway of Organic Pollutants Degradation and Proton Assisted Electron Transfer Mechanism of Cr(VI) Reduction. *Appl. Catal. B Environ.* **2017**, *207*, 17–26. [[CrossRef](#)]
31. Chang, F.; Zhang, X.; Yang, C.; Peng, S.; Hu, X. Ag Nanoparticles-Embellished Bi₁₂GeO₂₀ Composites: A Plasmonic System Featured with Reinforced Visible-Light Photocatalytic Performance and Ultra-Stability. *Appl. Surf. Sci.* **2020**, *527*, 146946. [[CrossRef](#)]

32. Chang, F.; Wang, X.; Zhao, S.; Zhang, X.; Hu, X. Fabrication of Bi₁₂GeO₂₀/Bi₂S₃ Hybrids with Surface Oxygen Vacancies by a Facile CS₂⁻-Mediated Manner and Enhanced Photocatalytic Performance in Water and Saline Water. *Sep. Purif. Technol.* **2022**, *287*, 120532. [[CrossRef](#)]
33. Wang, M.; Tan, G.; Dang, M.; Wang, Y.; Zhang, B.; Ren, H.; Lv, L.; Xia, A. Dual Defects and Build-in Electric Field Mediated Direct Z-Scheme W₁₈O₄₉/g-C₃N_{4-x} Heterojunction for Photocatalytic NO Removal and Organic Pollutant Degradation. *J. Colloid Interface Sci.* **2021**, *582*, 212–226. [[CrossRef](#)] [[PubMed](#)]
34. Zhang, Z.; Huang, J.; Fang, Y.; Zhang, M.; Liu, K.; Dong, B. A Nonmetal Plasmonic Z-Scheme Photocatalyst with UV- to NIR-Driven Photocatalytic Protons Reduction. *Adv. Mater.* **2017**, *29*, 1606688. [[CrossRef](#)]
35. Nie, Q.; Jia, L.; Luan, J.; Cui, Y.; Liu, J.; Tan, Z.; Yu, H. Graphene Quantum Dots/BiOCl Visible-Light Active Photocatalyst for Degradation of NO. *Chem. Eng. Sci.* **2024**, *285*, 119614. [[CrossRef](#)]
36. Yang, Y.; Mao, J.; Yin, D.; Zhang, T.; Liu, C.; Hao, W.; Wang, Y.; Hao, J. Synergy of S-Vacancy and Heterostructure in BiOCl/Bi₂S_{3-x} Boosting Room-Temperature NO₂ Sensing. *J. Hazard. Mater.* **2023**, *455*, 131591. [[CrossRef](#)]
37. Liu, W.; Li, J.; Zheng, J.; Song, Y.; Shi, Z.; Lin, Z.; Chai, L. Different Pathways for Cr(III) Oxidation: Implications for Cr(VI) Reoccurrence in Reduced Chromite Ore Processing Residue. *Environ. Sci. Technol.* **2020**, *54*, 11971–11979. [[CrossRef](#)]
38. Shan, Z.; Yang, Y.; Shi, H.; Zhu, J.; Tan, X.; Luan, Y.; Jiang, Z.; Wang, P.; Qin, J. Hollow Dodecahedra Graphene Oxide- Cuprous Oxide Nanocomposites with Effective Photocatalytic and Bactericidal Activity. *Front. Chem.* **2021**, *9*, 755836. [[CrossRef](#)]
39. Sun, L.; Jiang, Z.; Yuan, B.; Zhi, S.; Zhang, Y.; Li, J.; Wu, A. Ultralight and Superhydrophobic Perfluorooctyltrimethoxysilane Modified Biomass Carbonaceous Aerogel for Oil-Spill Remediation. *Chem. Eng. Res. Des.* **2021**, *174*, 71–78. [[CrossRef](#)]
40. Liu, W.; Zheng, J.; Ou, X.; Liu, X.; Song, Y.; Tian, C.; Rong, W.; Shi, Z.; Dang, Z.; Lin, Z. Effective Extraction of Cr(VI) from Hazardous Gypsum Sludge via Controlling the Phase Transformation and Chromium Species. *Environ. Sci. Technol.* **2018**, *52*, 13336–13342. [[CrossRef](#)]
41. Nadeem, M.S.; Baoji, M.; Alam, M.M.; Riaz, N.N.; Al-Sehemi, A.G.; Munawar, T.; Mukhtar, F.; Rabbani, A.W.; Naz, A.; Al-Tahan, M.A.; et al. Sr-Doped ZnO Thin Film on a Silicon Substrate (100) Grown by Sol-Gel Method: Structural and Optical Study. *Opt. Mater.* **2024**, *157*, 116106. [[CrossRef](#)]
42. Chang, F.; Li, J.; Kou, Y.; Bao, W.; Shi, Z.; Zhu, G.; Kong, Y. The Intense Charge Migration and Efficient Photocatalytic NO Removal of the S-Scheme Heterojunction Composites Bi₇O₉I₃-BiOBr. *Sep. Purif. Technol.* **2025**, *353*, 128402. [[CrossRef](#)]
43. Chang, F.; Bao, W.; Li, K.; Bai, W.; Shi, Z.; Liu, D.; Kong, Y. Augmented Photocatalytic NO Removal by the S-Scheme Bi₇O₉I₃/Bi₂S₃ Heterojunctions with Surface Oxygen Vacancies: Experimental Analyses and Theoretical Calculations. *J. Environ. Manag.* **2024**, *370*, 122390. [[CrossRef](#)]
44. Chang, F.; Zhao, S.; Lei, Y.; Wang, X.; Dong, F.; Zhu, G.; Kong, Y. Jointly Augmented Photocatalytic NO Removal by S-Scheme Bi₁₂SiO₂₀/Ag₂MoO₄ Heterojunctions with Surface Oxygen Vacancies. *J. Colloid Interface Sci.* **2023**, *649*, 713–723. [[CrossRef](#)]
45. Chang, F.; Yang, C.; Wang, X.; Zhao, S.; Wang, J.; Yang, W.; Dong, F.; Zhu, G.; Kong, Y. Mechanical Ball-Milling Preparation and Superior Photocatalytic NO Elimination of Z-Scheme Bi₁₂SiO₂₀-Based Heterojunctions with Surface Oxygen Vacancies. *J. Clean. Prod.* **2022**, *380*, 135167. [[CrossRef](#)]
46. Apriandanu, D.O.B.; Nakayama, S.; Shibata, K.; Amano, F. Ti-Doped Fe₂O₃ Photoanodes on Three-Dimensional Titanium Microfiber Felt Substrate for Photoelectrochemical Oxygen Evolution Reaction. *Electrochim. Acta* **2023**, *456*, 142434. [[CrossRef](#)]
47. Apriandanu, D.O.B.; Surya, R.M.; Beppu, K.; Amano, F. Anion-Exchange Membrane-Photoelectrochemical Water Splitting Using Porous Hematite Photoanodes. *ACS Appl. Energy Mater.* **2023**, *6*, 10736–10741. [[CrossRef](#)]
48. Oliveira, T.M.; Santos, C.; Lima, A.F.; Lalic, M.V. Antisite Defect as Rule for Photorefractive, Photochromic and Photocatalytic Properties of Bi₁₂MO₂₀ (M = Ge, Si, Ti) Sillenite Crystals. *J. Alloys Compd.* **2017**, *720*, 187–195. [[CrossRef](#)]
49. Wang, W.; Wen, C.; Guan, J.; Man, H.; Bian, J. Insight on Photocatalytic Oxidation of High Concentration NO over BiOCl/Bi₂WO₆ under Visible Light. *J. Ind. Eng. Chem.* **2021**, *103*, 305–313. [[CrossRef](#)]
50. Chang, F.; Wei, Z.; Zhao, Z.; Qi, Y.; Liu, D. 2D-2D Heterostructured Composites Bi₄O₅Br₂-SnS₂ with Boosted Photocatalytic NO_x Abatement. *J. Ind. Eng. Chem.* **2023**, *117*, 265–272. [[CrossRef](#)]
51. Chen, Q.; Long, H.; Chen, M.; Rao, Y.; Li, X.; Huang, Y. In Situ Construction of Biocompatible Z-Scheme α-Bi₂O₃/CuBi₂O₄ Heterojunction for NO Removal under Visible Light. *Appl. Catal. B Environ.* **2020**, *272*, 119008. [[CrossRef](#)]
52. Chang, F.; Wang, X.; Yang, C.; Li, S.; Wang, J.; Yang, W.; Dong, F.; Hu, X.; Liu, D.; Kong, Y. Enhanced Photocatalytic NO Removal with the Superior Selectivity for NO₂⁻/NO₃⁻ Species of Bi₁₂GeO₂₀-Based Composites via a Ball-Milling Treatment: Synergetic Effect of Surface Oxygen Vacancies and n-p Heterojunctions. *Compos. Part B* **2022**, *231*, 109600. [[CrossRef](#)]
53. Huo, W.; Xu, W.; Cao, Z.; Guo, Z.; Liu, X.; Ge, G.; Li, N.; Lan, T.; Yao, H.; Zhang, Y.; et al. Carbonate Doped Bi₂MoO₆ Hierarchical Nanostructure with Enhanced Transformation of Active Radicals for Efficient Photocatalytic Removal of NO. *J. Colloid Interface Sci.* **2019**, *557*, 816–824. [[CrossRef](#)] [[PubMed](#)]
54. Zha, R.; Niu, Y.; Liu, C.; He, L.; Zhang, M. Oxygen Vacancy Configuration in Confined BiVO₄-Bi₂S₃ Heterostructures Promotes Photocatalytic Oxidation of NO. *J. Environ. Chem. Eng.* **2021**, *9*, 106586. [[CrossRef](#)]

55. Liu, H.; Pan, L.; Nie, J.; Mei, H.; Zhu, G.; Jin, Z.; Cheng, L.; Zhang, L. Bi₁₂TiO₂₀-TiO₂ S-Scheme Heterojunction for Improved Photocatalytic NO Removal: Experimental and DFT Insights. *Sep. Purif. Technol.* **2023**, *314*, 123575. [[CrossRef](#)]
56. Wang, Z.; Huang, Y.; Ho, W.; Cao, J.; Shen, Z.; Lee, S. Fabrication of Bi₂O₂CO₃/g-C₃N₄ Heterojunctions for Efficiently Photocatalytic NO in Air Removal: In-Situ Self-Sacrificial Synthesis, Characterizations and Mechanistic Study. *Appl. Catal. B Environ.* **2016**, *199*, 123–133. [[CrossRef](#)]

Disclaimer/Publisher's Note: The statements, opinions and data contained in all publications are solely those of the individual author(s) and contributor(s) and not of MDPI and/or the editor(s). MDPI and/or the editor(s) disclaim responsibility for any injury to people or property resulting from any ideas, methods, instructions or products referred to in the content.